APPLIED PHYSICS

Electric field control of magnon spin currents in an antiferromagnetic insulator

Changjiang Liu[1†], Yongming Luo[1,2†], Deshun Hong[1], Steven S.-L. Zhang[1,3], Hilal Saglam[1], Yi Li[1], Yulin Lin[4], Brandon Fisher[4], John E. Pearson[1], J. Samuel Jiang[1], Hua Zhou[5], Jianguo Wen[4], Axel Hoffmann[1,6]*, Anand Bhattacharya[1]*

Pure spin currents can be generated via thermal excitations of magnons. These magnon spin currents serve as carriers of information in insulating materials, and controlling them using electrical means may enable energy efficient information processing. Here, we demonstrate electric field control of magnon spin currents in the antiferromagnetic insulator Cr_2O_3. We show that the thermally driven magnon spin currents reveal a spin-flop transition in thin-film Cr_2O_3. Crucially, this spin-flop can be turned on or off by applying an electric field across the thickness of the film. Using this tunability, we demonstrate electric field–induced switching of the polarization of magnon spin currents by varying only a gate voltage while at a fixed magnetic field. We propose a model considering an electric field–dependent spin-flop transition, arising from a change in sublattice magnetizations via a magnetoelectric coupling. These results provide a different approach toward controlling magnon spin current in antiferromagnets.

INTRODUCTION

In addition to electric charge, the spin degree of freedom of electrons can be used to carry and process information. Unlike electric currents, the transport of spins can be realized using magnon currents, without the associated Joule heating. Therefore, spintronics has the potential of serving as a building block for future generations of computing with low power dissipation (1, 2). An operational spintronic device consists of three integral parts: creating, manipulating, and detecting spin currents. Thanks to steady progress made over the past decade (2–5), several techniques have been explored for generating spin currents. Among them, using thermal excitations of magnons, an emerging field also known as spin caloritronics (3), has shown promise for producing pure spin currents. The underlying mechanism is understood in terms of the spin Seebeck effect (SSE) (6). Since its discovery, the SSE has been observed in diverse material systems that include ferrimagnetic (7), paramagnetic (8, 9), and antiferromagnetic materials (10, 11). This is primarily because thermal excitation of magnons does not require long-range magnetic order and coherent precession at resonance, both of which are necessary for other methods such as the spin-pumping effect (9, 12–14).

The next step toward realizing operational spin caloritronic devices is exploring ways, particularly via electrical means, to manipulate the spin current. In principle, both the amplitude (magnon density) and polarization vector of the thermally excited magnons could be manipulated for encoding information. However, experimental work in this area has been lacking thus far. One of the

challenges here is to establish an efficient coupling between magnons and external electric fields. For example, to control the magnon density, one would require a large change in spin-wave dispersions and/or magnetic anisotropies to be induced by an electric field (15, 16). In comparison, controlling the polarization vector of magnons could be more feasible (17), as the magnon polarization is often aligned with the magnetic order in the materials. A possible route toward this goal is to use magnetoelectric or multiferroic materials that are capable of both generating spin currents and, at the same time, allowing for interactions between spins and electric fields (18). Antiferromagnetic insulators can be a promising platform for this purpose. In addition to the benefits of low stray fields and potentially high operation speeds, they have recently been shown to be efficient systems for producing magnon spin currents using the SSE (19, 20). Furthermore, some antiferromagnets allow for a direct coupling between spins and an external electric field (21–23), owing to the unique symmetry of their magnetic lattices and correlations between spins and orbitals (24–26).

In this work, we demonstrate an electric field control of magnon spin currents using the antiferromagnetic insulator Cr_2O_3. We use the SSE to generate a magnon spin current, which is detected as a voltage using the inverse spin Hall effect (ISHE). We show that a spin-flop transition in thin-film Cr_2O_3 is revealed by a unique hysteretic SSE signal. Using micromagnetic simulations, we show that the line shape of the SSE signal precisely captures the orientations of the magnetic sublattices of Cr_2O_3 in response to magnetic fields. Moreover, we observe that the spin-flop transition in Cr_2O_3 films can be switched on or off by simply varying a gate voltage across the thickness of the film. Using this unique sensitivity of the spin-flop transition to electric fields, we show that the polarization of magnon spin currents can be switched by varying only the gate voltage while maintaining a fixed magnetic field. To explain our experimental observations, we have proposed a quantitative model that considers electric field–induced changes in the magnetization of individual sublattices based on a magnetoelectric coupling in Cr_2O_3. Further evidence of this explanation has been obtained in our temperature dependence measurements.

[1]Materials Science Division, Argonne National Laboratory, Lemont, IL 60439, USA. [2]School of Electronics and Information, Hangzhou Dianzi University, Hangzhou, Zhejiang 310018, China. [3]Department of Physics, Case Western Reserve University, Cleveland, OH 44106, USA. [4]Nanoscale Science and Technology Division, Argonne National Laboratory, Lemont, IL 60439, USA. [5]Advanced Photon Source, Argonne National Laboratory, Lemont, IL 60439, USA. [6]Department of Materials Science and Engineering and Materials Research Laboratory, University of Illinois at Urbana-Champaign, Urbana, IL 61801, USA.
*Corresponding author. Email: anand@anl.gov (A.B.); axelh@illinois.edu (A.H.)
†These authors contributed equally to this work.

RESULTS

Our devices that incorporate Cr_2O_3 films are fabricated on (0001) orientated Al_2O_3 substrate. Figure 1A shows the vertical structure of the device, which consists of Pt (5)/Cr_2O_3 (250)/Pt (5)/SiN_3 (100)/Pt (10), with the number indicating the thickness, in units of nanometers, of each layer along the growth direction. The two Pt layers grown at the bottom and top surfaces of the Cr_2O_3 serve as spin detectors and electrodes for applying a gate voltage, which is illustrated in Fig. 1A. The SiN_3 layer electrically isolates the on-chip heater (Pt) grown on the top. More details of the sample growth and fabrication are presented in Materials and Methods.

In zero magnetic field, the two antiferromagnetically coupled magnetic sublattices in Cr_2O_3 are collinear with the c axis, which is equivalent to the z-direction of our measurement geometry (see Fig. 1, A and B). In the SSE experiment, a sinusoidal electrical current with a low frequency of 3 Hz is applied through the heater, which generates a temperature gradient in the vertical direction as indicated by the red arrow in Fig. 1A. Thermally excited magnons inside Cr_2O_3 propagate toward/away from the two Cr_2O_3/Pt interfaces, where magnons are converted into spin current carried by conduction electrons in Pt (Fig. 1C), in which a transverse voltage V_{SSE} develops via the ISHE. When a large magnetic field is applied in a direction other than the c axis, the orientations of two magnetic sublattices are forced to tilt, which is illustrated in Fig. 1C. Shown in

Fig. 1D are structural characterizations of the Cr_2O_3 on the SSE devices using a focused x-ray beam with micrometer length scale. The beam was directed to different areas of the sample with fabricated SSE devices. In the area containing the Pt layer, the Cr_2O_3 Bragg peak is seen as a bump overlaid on the broad Pt signal. The position of the bump matches the Cr_2O_3 Bragg peak measured in the region where the Pt layer was milled away, as indicated by the vertical dashed line. Our high-resolution transmission electron microscopy (HRTEM) measurement shown in Fig. 1E further confirms the good crystallinity of Cr_2O_3 films in these SSE devices.

Spin-flop transition in thin-film Cr_2O_3

Our SSE measurements show clear signs of a spin-flop transition in the Cr_2O_3 films, which is verified by micromagnetic simulations. Shown in Fig. 2 (A and B) are the angular dependence measurements of SSE using the bottom Pt spin detector at magnetic fields of different amplitudes. The direction of magnetic field, θ_H, measured from the z axis, is rotated in the x-z plane relative to the sample. As seen in Fig. 2A, the magnitude of the SSE voltage increases gradually from 0 nV to a maximum as θ_H increases. The SSE signal then decreases smoothly to zero and changes sign as the θ_H goes through 180°. The sign change in the SSE is expected from the ISHE. Also seen in Fig. 2A is that the maximum of the SSE occurs at higher θ_H (closer to 180°) as the amplitude of magnetic field increases. For the
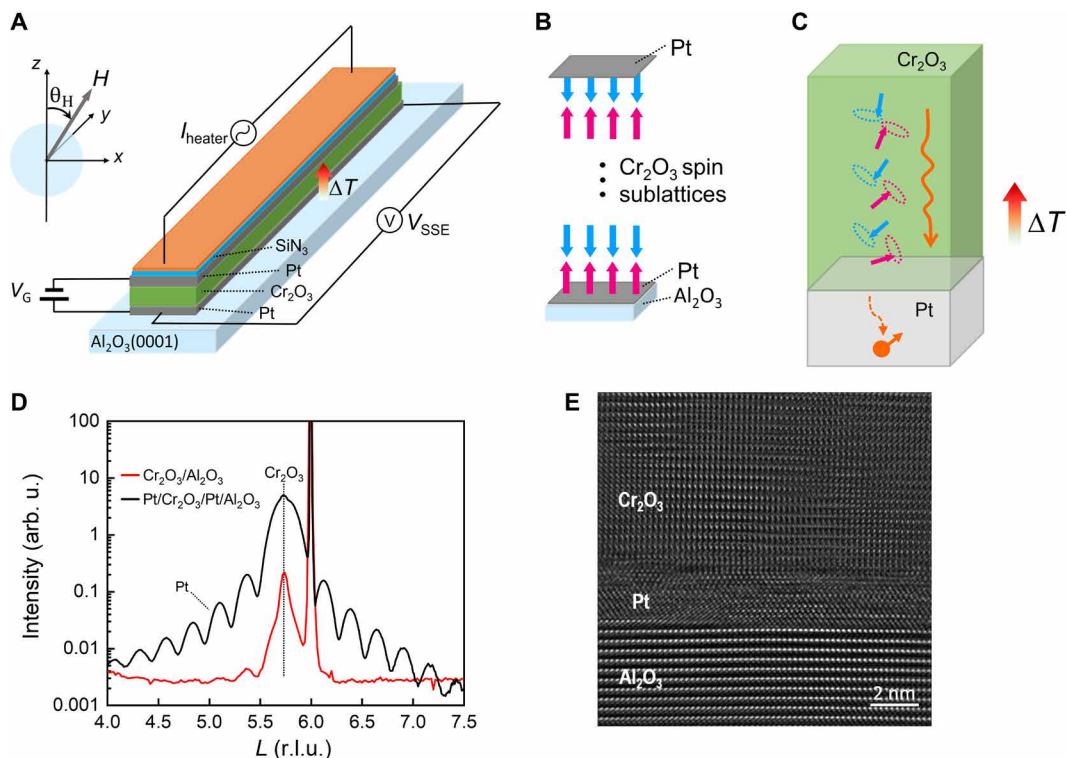

Fig. 1. Device design, measurement geometry, and sample characterizations. (**A**) Schematics of the SSE device showing the vertical structure of the sample. The direction of the magnetic field is varied in the x-z plane, and the spin Seebeck voltage V_{SSE} develops in the y-direction. Gate voltage is applied across the thickness of Cr_2O_3 (positive electric field is defined as pointing from the substrate to the film) (**B**) The sublattice colored in red and blue is in contact with the bottom and top Pt in the SSE device, respectively. (**C**) Magnon spin currents created by thermal excitations in Cr_2O_3 (under a tilted magnetic field) propagates toward the Cr_2O_3/Pt interface (orange wiggly arrow), where it is converted into a spin current (dashed arrow) carried by conduction electrons in the Pt layer. (**D**) Specular 00L x-ray diffraction data (H, $K = 0$) for the SSE device near $L = 6$, in reciprocal lattice units (r.l.u.), of Al_2O_3. Measurement in areas with and without the Pt layer is shown in black and red, respectively. (**E**) HRTEM characterization near the bottom Cr_2O_3/Pt/Al_2O_3 interface. We note that the HRTEM was taken in an area near the edge of the Pt strip, and so the thickness of Pt seen in (E) is less than 5 nm.
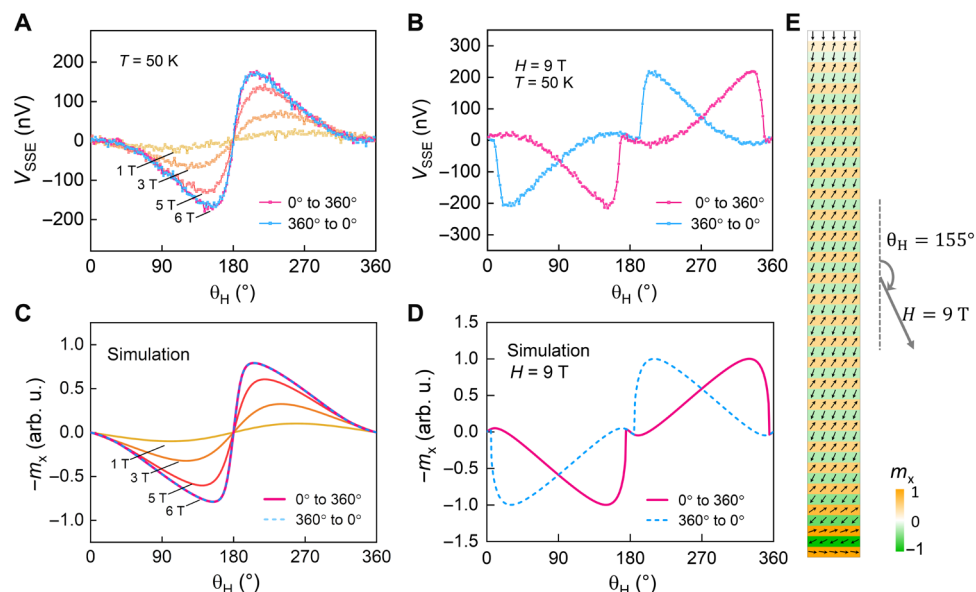
Fig. 2. SSE measurements and simulations at different magnetic fields. (**A**) Angular dependence of SSE measurements in a range of magnetic fields, which are below the surface spin-flop field. The data obtained during field rotations of opposite directions fall on top of each other, as shown by the measurement at 6 T. (**B**) Measurement at magnetic field of 9 T, above the spin-flop field, shows hysteretic curve with sharp jumps in the SSE signal. (**C** and **D**) Micromagnetic simulations at low and high magnetic fields, respectively, which obtain largely the same line shape of the SSE data observed in the experiment. (**E**) An example of spin structures along the thickness of the film obtained in the simulation for $H = 9$ T and $\theta_H = 155°$. Note that the spin orientations vary gradually along the z-direction.

measurement at $H = 6$ T, data corresponding to θ_H rotated in the clockwise (0° to 360°) and counterclockwise (360° to 0°) directions are shown in red and blue, respectively. The shape of the curve remains the same regardless of the direction of rotation of the magnetic field (red and blue data overlap). This is the case for all measurements at lower magnetic fields. Notably, as the magnetic field is increased further, distinct difference in the angular dependences of V_{SSE} are observed, which is shown in Fig. 2B for $H = 9$ T. The data $V_{SSE}(\theta_H)$ display an abrupt jump near $\theta_H = 0°$ or 180° (easy axis of the Néel axis) and hysteretic behavior—red and blue traces are completely separated when θ_H is rotated in opposite directions.

The SSE signal measured from the Pt spin detector, in general, depends on two physical quantities: the density and the polarization vector of the magnons (27). In the present case, the number of magnons is mostly fixed as the heater power in our measurement is constant. The polarization vector of the magnons is, however, determined by the unit vector of the magnetization of the sublattices of Cr_2O_3 (12, 28). We confirmed that the SSE signal mainly comes from bulk magnons through the observation of a large suppression of the SSE voltage by magnon excitation gap in bulk Cr_2O_3 at temperatures below 7 K. The details will be discussed elsewhere. As shown in Fig. 1B, an individual layer of spins in the (0001) surface of Cr_2O_3 is uncompensated, which sets the quantization axis for the thermally driven magnons reaching the Cr_2O_3/Pt interface and also the spin current induced in the Pt layer. In our measurement geometry (Fig. 1A), the V_{SSE} produced from the ISHE is in the y-direction. Therefore, we expect that the angular dependence of the V_{SSE} to be proportional to the x-component of the spins in the two end layers of Cr_2O_3, as discussed in more detail in our recent work (29).

To verify the above scenario, we have performed micromagnetic simulations of the response of the magnetic sublattices to a rotating magnetic field, as shown in (29). We consider the finite thickness of

the Cr_2O_3, i.e., spins in the surface layers have reduced number of exchange-coupled neighbors than those in the bulk (30, 31) (see also note S1). On the basis of this model, the angular dependent V_{SSE} curves shown in Fig. 2 (A and B) are reproduced by plotting the x-component of the magnetization in the surface layer, which are shown in Fig. 2 (C and D, respectively). The hysteretic $V_{SSE}(\theta_H)$ seen in Fig. 2B occurs when spins near the surface are driven into a flopped state—Néel axis being mostly perpendicular to the large magnetic field. Those spins rotate beyond the magnetic hard plane as θ_H increases further. In contrast, when the magnetic field is low, the magnetic sublattices are unable to overcome the magnetic anisotropy energy, and the orientations of the sublattice spins only tilt around the easy axis, producing a nonhysteretic V_{SSE} response. Shown in Fig. 2E is an example in which spins near the bottom surface are flopped and are about to rotate beyond the magnetic hard plane. This corresponds to the state where the SSE signal in Fig. 2B is the maximum (the red trace at $\theta_H = 155°$). More details of the simulations and measurement results, including using the top Pt spin detector and the spin-flop transition detected in a magnetic-field sweep, are presented in note S1 and figs. S1 to S3.

Electric field–dependent spin-flop transition

Our devices using thin-film Cr_2O_3 allow the investigation of electric field control of the V_{SSE} by applying a gate voltage (V_G) across the film's thickness. We observe that applying a V_G can effectively control the spin-flop transition and, in turn, the response of V_{SSE}. Shown in Fig. 3 are the measurements of SSE under different V_G with magnetic field fixed at 8.5 T. At $V_G = 0$ V (Fig. 3A), the V_{SSE} shows partial switching/hysteretic behavior, which is presumably due to the existence of domains in the Cr_2O_3 film (32) caused by spatial variations in anisotropy energies, and also that the system is on the verge of a spin-flop transition. Notably, when a finite V_G is applied, without
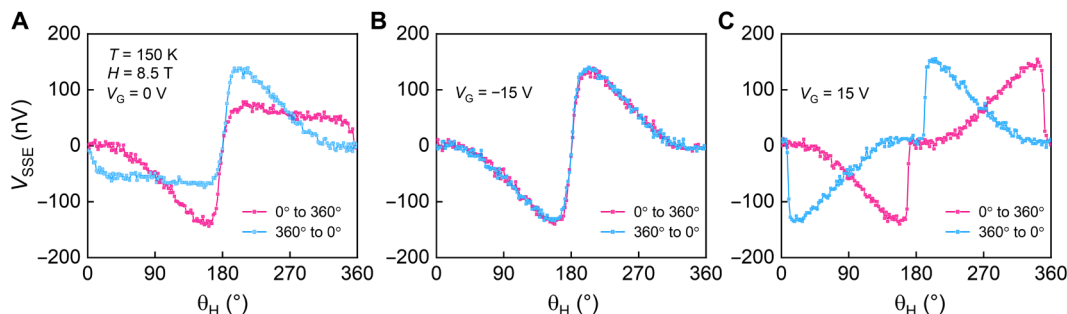
Fig. 3. Gate voltage control of spin-flop transition. (**A**) Angular dependence of the V_{SSE} measured at $H = 8.5$ T, in the vicinity of spin-flop transition, under zero gate voltage. (**B**) When a negative gate voltage of -15 V is applied, the SSE response becomes fully reversible with respect to the rotation of the magnetic field. (**C**) Under a positive gate voltage of 15 V, the SSE signal becomes completely hysteretic, which is similar to measurement results at higher magnetic field.

changing the amplitude of the magnetic field, the angular response of V_{SSE} is completely changed. Shown in Fig. 3 (B and C) are the measurement results under a negative and positive V_G, respectively. The curve $V_{SSE}(\theta_H)$ under $V_G = -15$ V becomes continuous and fully reversible with respect to the rotation of the magnetic field. The line shape is similar to the result measured at lower magnetic field as seen in Fig. 2A. In contrast, when a positive $V_G = 15$ V is applied, the $V_{SSE}(\theta_H)$ curve shows sharp jumps when θ_H is near 0° or 180°, resulting in a fully hysteretic behavior when θ_H is rotated in opposite directions—a line shape similar to that shown in Fig. 2B. These observations demonstrate that applying an electric field has a decisive control of the dynamics of the magnetic sublattices in Cr_2O_3, which turns the polarization of the thermally excited magnon spin current.

Controlling spin currents using an electric field

The tunability of spin-flop transition by V_G suggests that we can control spin currents by using only an electric field while keeping the magnetic field fixed. To accomplish this, we first obtain the angular dependences of V_{SSE} near the spin-flop transition under a range of gate voltages, which are shown in Fig. 4A. The critical magnetic field angle θ_c where V_{SSE} displays a steep rise shows a strong dependence on V_G. When V_G is positive, θ_c is driven to lower values (easy to switch), and the transition becomes sharper. For example, θ_c is reduced by over 10° with an application of a $V_G = 24$ V. Here, θ_c is determined at θ_H where the change in V_{SSE} is half of its maximum, as illustrated by $\Delta\theta_c$ in the figure. In contrast, applying negative V_G produces the opposite effect, i.e., the transition in V_{SSE} is hindered—with the θ_c pushed to higher values.

We next fix the orientation of the magnetic field at a value of θ_H, which is within the range where θ_c is tunable by the electric field as shown in Fig. 4A. Shown in Fig. 4B are the measured SSE signals as a function of V_G for magnetic field applied along three different θ_H. In this measurement, θ_H is approached by rotating the magnetic field from 0° under a negative V_G. The V_G is then gradually increased to positive values. We observe a voltage-driven transition in V_{SSE}, as indicated by the black arrow in Fig. 4B, arising from the rotation of magnetic sublattices that changes the polarization of magnons. We note that because of a leakage current through the Cr_2O_3 film, a magnetization configuration–independent background voltage has been subtracted from the raw data (see fig. S4). As shown in Fig. 4B, V_{SSE} rises from about -150 to 0 nV as V_G increases from 15 to 22 V at $\theta_H = 163°$. When θ_H is set to higher angles [closer to $\theta_c(V_G = 0 \text{ V})$], the threshold V_G required for the transition of V_{SSE} becomes lower, which are shown by the yellow and blue data points.

These measurements thus demonstrate an electric field control of magnon spin currents in the antiferromagnetic insulator Cr_2O_3.

Model and temperature dependence measurement

The operation of the electric field control of the SSE presented above may be understood on the basis of the magnetoelectric coupling in Cr_2O_3. Figure 5A shows the lattice and spin structures of Cr_2O_3 in a primitive cell along the c axis. Adjacent Cr^{3+} ions are separated by either two ligand O^{2-} triangles or just a single O^{2-} triangle, with the former having slightly longer bond length between O^{2-}. The application of an electric field along the c axis will drive those Cr^{3+} ions on one sublattice (shown with red spins) closer to the double O^{2-} triangle and away from the single one, while the displacement of the Cr^{3+} ions on the other sublattice (shown with blue spins) relative to their ligand O^{2-} triangles are opposite (*33*). These changes in bond lengths between the Cr^{3+} and ligand O^{2-} ions break the equivalence of the two magnetic sublattices (*34*), which induces a net magnetization $\Delta m = \alpha_{zz}E_z$, where α_{zz} is the diagonal component of the linear magnetoelectric coefficient and E_z is z-component of the electric field (*35–39*). To more clearly illustrate the electric field–induced rotation of the sublattices, we propose that under a positive (negative) electric field, the absolute magnitude of the magnetic moment of the sublattice A, shown with red arrows in Fig. 5A, would increase (decrease); while the magnetic moment of the sublattice B would decrease (increase), regardless of the orientation of their spins. In other words, the electric field gives rise to an effective ferrimagnetic spin configuration. We note that, under this scenario, the sign of α_{zz} is dependent on the orientations of the two sublattices, which is consistent with experimental findings, i.e., configuration of Fig. 5A corresponds to a positive α_{zz} (*40*).

Figure 5B illustrates how the switching of the magnetic sublattices is induced by an electric field. To get a clear understanding of the different behaviors under a positive and negative gate voltages, as shown in Fig. 3, we also need to consider that the Cr_2O_3 films in our SSE devices are slightly "ferrimagnetic". Our magnetic field–cooling and angular dependence measurements of SSE suggest that the sublattice A in contact with the bottom Pt layer carry an extra magnetization m'. The m' can come from excess Cr atoms formed at the bottom Cr_2O_3/Pt interface resulting from misfit dislocations during the heteroepitaxial film growth, as observed in a previous study (*41*). More details on the subtle difference between the sublattices A and B, including effect of magnetic anisotropies, are presented in note S2. Under a positive electric field, as shown in Fig. 5B, the increased (decreased) magnetization $\Delta m/2$ in the sublattice A (B) from the
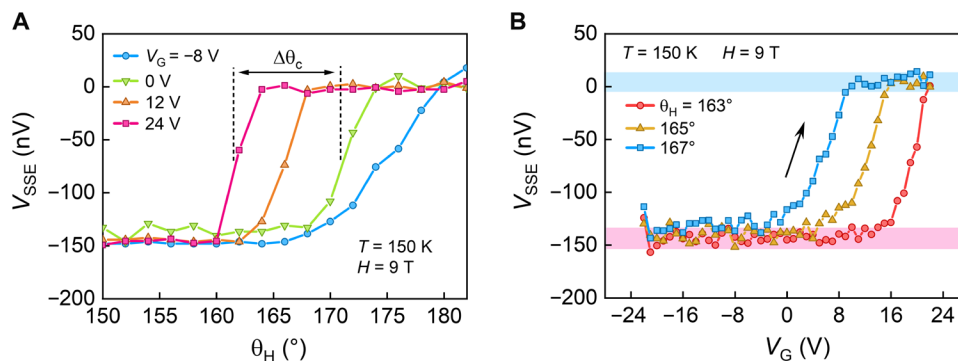
Fig. 4. Gate voltage control of magnon spin currents. (**A**) Angular dependence of V_{SSE} measured near the spin-flop transition under different gate voltages. (**B**) Transition of V_{SSE} driven by the gate voltage under a fixed magnetic field applied at along three different angles. V_{SSE} is driven to rise from about −150 to 0 nV with the increase of V_G.
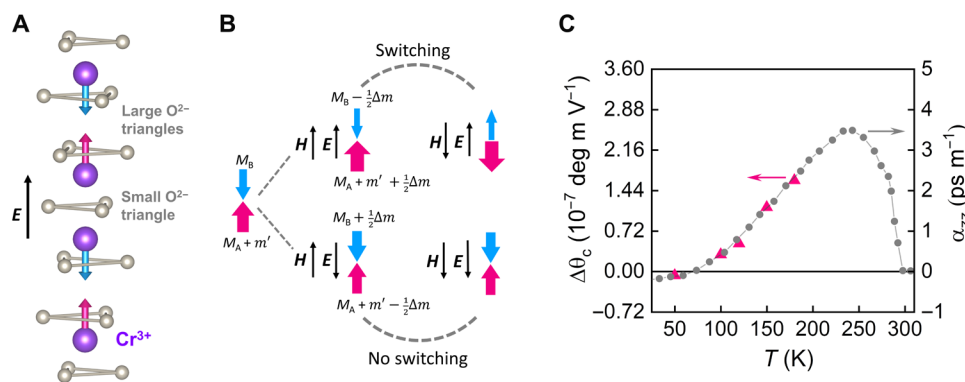

Fig. 5. Cr$_2$O$_3$ lattice structure and magnetoelectric manipulation of the magnetic sublattices. (**A**) Spin structure of Cr^{3+} in a rhombohedral cell of Cr_2O_3. The two magnetic sublattices are shown by red and blue arrows, respectively. (**B**) Illustration of the electric field–induced switching of the magnetic sublattices via the magneto-electric coupling. M_A (M_B) is the magnetization of the sublattice. Application of an electric field along the *c* axis increases (decreases) their magnitude by $\Delta m/2$, which is illustrated by the width of the arrows. In addition, the Cr spins at the bottom Cr_2O_3/Pt interface, belonging to sublattice A, carries an extra magnetization m'. With the application of a magnetic field, the magnetic sublattices reorient themselves to lower the total magnetic energy. In a positive electric field (upper part), the switching process is aided by the magnetoelectric-induced magnetic moment. Conversely, a negative electric field (lower part) makes it harder to switch the magnetic sublattices. (**C**) Temperature dependence of the change of θ_c normalized by the electric field (left axis) and the magnetoelectric coefficient α_{zz} of Cr_2O_3 (right axis). The data of α_{zz} are reproduced from (*40*).

magnetoelectric effect produces a net magnetization Δm that, adding to m', allows the magnetic lattices to rotate or switch more readily in response to the rotation of magnetic field to lower the total Zeeman energy (Fig. 3C). Under a negative gate voltage, however, the magnetoelectric-induced magnetization Δm opposes the extra magnetization m'. As shown in the lower part of Fig. 5B, when Δm is smaller than or comparable to m', the switching process is hindered because the energy gain from the Zeeman interaction would be less than the cost of magnetic anisotropy energy, resulting in the behavior seen in Fig. 3B.

To obtain further experimental evidence that the magnetoelectric coupling in Cr_2O_3 is responsible for the electric field tunability of SSE, we have performed temperature dependence measurements. Shown in Fig. 5C is the change in transition angle $\Delta\theta_c$, as illustrated in Fig. 4A, normalized by the electric field at different temperatures. $\Delta\theta_c$ is considerably reduced at temperatures below 100 K, and it further changes sign at 50 K. We note that the symbol size in the plot is larger than the uncertainty for the data points (see also fig. S5). This temperature dependence of $\Delta\theta_c$ follows closely the temperature-dependent magnetoelectric coefficient α_{zz} of Cr_2O_3, which is shown on the right axis of Fig. 5C (*40*).

We have carried out a quantitative analysis of how the spin-flop field depends on an electric field (note S3). We express the magnetic energy density using a macrospin approximation (*42*)

$$\varepsilon_M = -\mathbf{H} \cdot (\mathbf{M}_A + \mathbf{M}_B) - (H_K/2M_s)(M_A\sin^2\theta_A + M_B\sin^2\theta_B) + (H_J/M_s)(\mathbf{M}_A \cdot \mathbf{M}_B)$$

where $\mathbf{H}$, H_K, and H_J are the applied magnetic field, effective anisotropy, and exchange fields, respectively; $\mathbf{M}_A$ ($\mathbf{M}_B$) is the magnetization of sublattice A (B); M_s is the saturation magnetization of one sublattice, and θ_A (θ_B) is the angle of $\mathbf{M}_A$ ($\mathbf{M}_B$) measured relative to the *z* axis. The change in spin-flop transition field is obtained by calculating how the magnetic energy density is modified near the spin-flopped state when the relative magnitude of $\mathbf{M}_A$ ($\mathbf{M}_B$) changes resulting from the magnetoelectric coupling. Experimentally, the change in spin-flop field induced by an electric field is determined from $\Delta\theta_c$—the difference in the longitudinal component of the applied magnetic field. Our model calculation predicts a value of $\Delta\theta_c$ that is within order of magnitude consistent with experimental results, the details of which are presented in note S3.

DISCUSSION

In conclusion, we have demonstrated an electric field control of magnon spin currents using antiferromagnetic Cr_2O_3 thin films. We have shown that the polarization vector of the antiferromagnetic magnons can be switched electrically, owing to an electric field–dependent spin-flop transition in Cr_2O_3. Our model and temperature dependence measurement suggest that this electrical tunability arises from the magnetoelectric coupling in Cr_2O_3. It is further possible to achieve a reversible electrical control of spin currents by reducing the leakage current and the boundary magnetization m' in Cr_2O_3 films. For example, it has been shown that using a seed layer V_2O_3 for the growth of Cr_2O_3 could yield a much smaller m', owing to a close lattice match between Cr_2O_3 and V_2O_3 (41). In addition, many of the antiferromagnetic insulators also have multiferroic properties. Incorporating those materials may allow for more efficient electrical control of the thermally excited magnons. The present work opens a different avenue for controlling spin currents in antiferromagnets, creating exciting prospects for applications of antiferromagnetic spintronic devices.

MATERIALS AND METHODS

Multiple samples are fabricated and measured during the course of this work (see table S1). The fabrication of the SSE devices involves several steps of patterning and materials growths. Al_2O_3 substrate is first annealed at 850°C under a chamber pressures of $\sim 3 \times 10^{-8}$ torr for 30 min. A 5-nm Pt layer is then grown at 400°C using dc sputtering. The sample is then transferred out of the chamber to pattern the Pt layer into Hall bars using photolithography and ion milling. After that, the sample is loaded back into the growth chamber and annealed at 700°C in vacuum for 30 min. Cr_2O_3 films with varying thicknesses are then grown using radio frequency reactive sputtering with a pure Cr target and an oxygen partial pressure of $\sim 5 \times 10^{-5}$ torr at 600°C. This is followed by a 5-nm Pt layer deposited at room temperature. In some cases, a 1.5-nm Cu is grown between Cr_2O_3 and the top Pt layer, which is used to examine a possible anomalous Nernst effect arising from proximity-induced ferromagnetism in Pt (see fig. S6). The Cu layer is also required for the observation of sublattice dynamics in the Pt layer on top of Cr_2O_3 (see figs. S1 and S2). Photolithography and ion milling are then used to define the upper Pt layer. A final step of patterning and liftoff are used to make a 100-nm-thick insulating SiN_3 and a 10-nm Pt heater wire.

The typical root mean square heater power at $T = 150$ K is 5 mW, corresponding to a power density of 1.9×10^5 W m^{-2}. The temperature difference between the top and bottom surface of the 250-nm Cr_2O_3 is $\Delta T \sim 0.9$ K. Synchrotron x-ray thin-film diffraction is carried out at the beamline sector 12-ID-D at Advanced Photon Source in Argonne National Laboratory. The x-ray beam is focused below 10 μm to probe local areas of the patterned SSE devices. The micromagnetic simulation presented in this work was performed using the Object Oriented MicroMagnetic Framework (43).

SUPPLEMENTARY MATERIALS

Supplementary material for this article is available at https://science.org/doi/10.1126/sciadv.abg1669

REFERENCES AND NOTES

1. A. Hoffmann, S. D. Bader, Opportunities at the frontiers of spintronics. *Phys. Rev. Appl.* **4**, 047001 (2015).
2. A. V. Chumak, V. I. Vasyuchka, A. A. Serga, B. Hillebrands, Magnon spintronics. *Nat. Phys.* **11**, 453–461 (2015).
3. G. E. W. Bauer, E. Saitoh, B. J. van Wees, Spin caloritronics. *Nat. Mater.* **11**, 391–399 (2012).
4. A. Hoffmann, Spin Hall effects in metals. *IEEE Trans. Magn.* **49**, 5172–5193 (2013).
5. R. Takahashi, M. Matsuo, M. Ono, K. Harii, H. Chudo, S. Okayasu, J. Ieda, S. Takahashi, S. Maekawa, E. Saitoh, Spin hydrodynamic generation. *Nat. Phys.* **12**, 52–56 (2016).
6. K. Uchida, J. Xiao, H. Adachi, J. Ohe, S. Takahashi, J. Ieda, T. Ota, Y. Kajiwara, H. Umezawa, H. Kawai, G. E. W. Bauer, S. Maekawa, E. Saitoh, Spin Seebeck insulator. *Nat. Mater.* **9**, 894–897 (2010).
7. K. Uchida, H. Adachi, T. Ota, H. Nakayama, S. Maekawa, E. Saitoh, Observation of longitudinal spin-Seebeck effect in magnetic insulators. *Appl. Phys. Lett.* **97**, 172505 (2010).
8. S. M. Wu, J. E. Pearson, A. Bhattacharya, Paramagnetic spin Seebeck effect. *Phys. Rev. Lett.* **114**, 186602 (2015).
9. C. Liu, S. M. Wu, J. E. Pearson, J. S. Jiang, N. d'Ambrumenil, A. Bhattacharya, Probing short-range magnetic order in a geometrically frustrated magnet by means of the spin Seebeck effect. *Phys. Rev. B* **98**, 060415 (2018).
10. S. Seki, T. Ideue, M. Kubota, Y. Kozuka, R. Takagi, M. Nakamura, Y. Kaneko, M. Kawasaki, Y. Tokura, Thermal generation of spin current in an antiferromagnet. *Phys. Rev. Lett.* **115**, 266601 (2015).
11. S. M. Wu, W. Zhang, A. KC, P. Borisov, J. E. Pearson, J. S. Jiang, D. Lederman, A. Hoffmann, A. Bhattacharya, Antiferromagnetic Spin Seebeck effect. *Phys. Rev. Lett.* **116**, 097204 (2016).
12. J. Xiao, G. E. W. Bauer, K. Uchida, E. Saitoh, S. Maekawa, Theory of magnon-driven spin Seebeck effect. *Phys. Rev. B* **81**, 214418 (2010).
13. R. Cheng, J. Xiao, Q. Niu, A. Brataas, Spin pumping and spin-transfer torques in antiferromagnets. *Phys. Rev. Lett.* **113**, 057601 (2014).
14. J. Li, C. B. Wilson, R. Cheng, M. Lohmann, M. Kavand, W. Yuan, M. Aldosary, N. Agladze, P. Wei, M. S. Sherwin, J. Shi, Spin current from sub-terahertz-generated antiferromagnetic magnons. *Nature* **578**, 70–74 (2020).
15. B. Rana, Y. Otani, Towards magnonic devices based on voltage-controlled magnetic anisotropy. *Commun. Phys.* **2**, 90 (2019).
16. P. Rovillain, R. de Sousa, Y. Gallais, A. Sacuto, M. A. Méasson, D. Colson, A. Forget, M. Bibes, A. Barthélémy, M. Cazayous, Electric-field control of spin waves at room temperature in multiferroic BiFeO3. *Nat. Mater.* **9**, 975–979 (2010).
17. A. M. Kuzmenko, D. Szaller, T. Kain, V. Dziom, L. Weymann, A. Shuvaev, A. Pimenov, A. A. Mukhin, V. Y. Ivanov, I. A. Gudim, L. N. Bezmaternykh, A. Pimenov, Switching of magnons by electric and magnetic fields in multiferroic borates. *Phys. Rev. Lett.* **120**, 027203 (2018).
18. C. A. F. Vaz, Electric field control of magnetism in multiferroic heterostructures. *J. Phys. Condens. Matter* **24**, 333201 (2012).
19. V. Baltz, A. Manchon, M. Tsoi, T. Moriyama, T. Ono, Y. Tserkovnyak, Antiferromagnetic spintronics. *Rev. Mod. Phys.* **90**, 015005 (2018).
20. M. B. Jungfleisch, W. Zhang, A. Hoffmann, Perspectives of antiferromagnetic spintronics. *Phys. Lett. A* **382**, 865–871 (2018).
21. C. Song, B. Cui, F. Li, X. Zhou, F. Pan, Recent progress in voltage control of magnetism: Materials, mechanisms, and performance. *Prog. Mater. Sci.* **87**, 33–82 (2017).
22. M. Street, W. Echtenkamp, T. Komesu, S. Cao, P. A. Dowben, C. Binek, Increasing the Néel temperature of magnetoelectric chromia for voltage-controlled spintronics. *Appl. Phys. Lett.* **104**, 222402 (2014).
23. W. Echtenkamp, C. Binek, Electric control of exchange bias training. *Phys. Rev. Lett.* **111**, 187204 (2013).
24. D. Khomskii, Classifying multiferroics: Mechanisms and effects. *Phys. Ther.* **2**, (2009).
25. M. Fiebig, T. Lottermoser, D. Meier, M. Trassin, The evolution of multiferroics. *Nat. Rev. Mater.* **1**, 16046 (2016).
26. A. Pimenov, A. A. Mukhin, V. Y. Ivanov, V. D. Travkin, A. M. Balbashov, A. Loidl, Possible evidence for electromagnons in multiferroic manganites. *Nat. Phys.* **2**, 97–100 (2006).
27. Y. Nambu, J. Barker, Y. Okino, T. Kikkawa, Y. Shiomi, M. Enderle, T. Weber, B. Winn, M. Graves-Brook, J. M. Tranquada, T. Ziman, M. Fujita, G. E. W. Bauer, E. Saitoh, K. Kakurai, Observation of magnon polarization. *Phys. Rev. Lett.* **125**, 027201 (2020).
28. S. M. Rezende, R. L. Rodríguez-Suárez, A. Azevedo, Theory of the spin Seebeck effect in antiferromagnets. *Phys. Rev. B* **93**, 014425 (2016).
29. Y. Luo, C. Liu, H. Saglam, Y. Li, W. Zhang, S. S.-L. Zhang, J. E. Pearson, B. Fisher, T. Zhou, A. Bhattacharya, A. Hoffmann, Distinguishing antiferromagnetic spin sublattices via the spin Seebeck effect. *Phys. Rev. B* **103**, L020401 (2021).
30. D. L. Mills, Surface spin-flop state in a simple antiferromagnet. *Phys. Rev. Lett.* **20**, 18–21 (1968).
31. R. W. Wang, D. L. Mills, E. E. Fullerton, J. E. Mattson, S. D. Bader, Surface spin-flop transition in Fe/Cr(211) superlattices: Experiment and theory. *Phys. Rev. Lett.* **72**, 920–923 (1994).
32. P. Appel, B. J. Shields, T. Kosub, N. Hedrich, R. Hübner, J. Faßbender, D. Makarov, P. Maletinsky, Nanomagnetism of magnetoelectric granular thin-film antiferromagnets. *Nano Lett.* **19**, 1682–1687 (2019).

33. M. Fiebig, Revival of the magnetoelectric effect. *J. Phys. D Appl. Phys.* **38**, R123–R152 (2005).

34. T. Nozaki, M. Sahashi, Magnetoelectric manipulation and enhanced operating temperature in antiferromagnetic Cr_2O_3 thin film. *Jpn. J. Appl. Phys.* **57**, 0902A2 (2018).

35. S. Shi, A. L. Wysocki, K. D. Belashchenko, Magnetism of chromia from first-principles calculations. *Phys. Rev. B* **79**, 104404 (2009).

36. M. Mostovoy, A. Scaramucci, N. A. Spaldin, K. T. Delaney, Temperature-dependent magnetoelectric effect from first principles. *Phys. Rev. Lett.* **105**, 087202 (2010).

37. A. Malashevich, S. Coh, I. Souza, D. Vanderbilt, Full magnetoelectric response of Cr_2O_3 from first principles. *Phys. Rev. B* **86**, 094430 (2012).

38. I. E. Dzyaloshinskii, On the magneto-electrical effects in antiferromagnets. *J. Exp. Theor. Phys.* **10**, 628 (1960).

39. D. N. Astrov, On the magneto-electrical effects in antiferromagnets. *Sov. Phys. JETP* **11**, 780 (1960).

40. P. Borisov, T. Ashida, T. Nozaki, M. Sahashi, D. Lederman, Magnetoelectric properties of 500-nmCr_2O_3 films. *Phys. Rev. B* **93**, 174415 (2016).

41. T. Kosub, M. Kopte, R. Hühne, P. Appel, B. Shields, P. Maletinsky, R. Hübner, M. O. Liedke, J. Fassbender, O. G. Schmidt, D. Makarov, Purely antiferromagnetic magnetoelectric random access memory. *Nat. Commun.* **8**, 13985 (2017).

42. S. Foner, High-field antiferromagnetic resonance in Cr_2O_3. *Phys. Rev.* **130**, 183–197 (1963).

43. M. J. Donahue, D. G. Porter, OOMMF user's guide, version 1.0. Interagency Report NISTIR 6376, (1999).

Citation: C. Liu, Y. Luo, D. Hong, S. S.-L. Zhang, H. Saglam, Y. Li, Y. Lin, B. Fisher, J. E. Pearson, J. S. Jiang, H. Zhou, J. Wen, A. Hoffmann, A. Bhattacharya, Electric field control of magnon spin currents in an antiferromagnetic insulator. *Sci. Adv.* **7**, eabg1669 (2021).